Journal of Materials Chemistry A

ROYAL SOCIETY OF CHEMISTRY

PAPER

View Article Online
View Journal

Cite this: DOI: 10.1039/d0ta02439b

Cathodic electrochemical deposition: a new strategy to enhance the activity and stability of silver cathodes for thin-film solid oxide fuel cells†

Hyunseung Kim, Han Gil Seo, ‡ Yoonseok Choi, § Dae-Kwang Lim and WooChul Jung *

Received 2nd March 2020
Accepted 28th April 2020

DOI: 10.1039/d0ta02439b

rsc.li/materials-a

Thin-film-based solid oxide fuel cells with reduced electrolyte thickness have been developed in an effort to lower the operating temperatures and increase the cost competitiveness and lifetime of the devices. Although silver has gained a considerable amount of attention as a cathode material with excellent oxygen reduction activity at lower temperatures, thermal instability due to agglomeration is a major disadvantage associated with the use of silver. Many oxide coating methods have been suggested to overcome this problem, but the results remain unsatisfactory. Here, we propose cathodic electrochemical deposition (CELD) as a new strategy to improve the activity and stability of silver electrodes. Pr-doped ceria is coated onto a nanoporous silver film by CELD and analyzed by electron microscopy, mass spectrometry, and X-ray diffraction. AC impedance spectroscopy of symmetric cells (electrode|electrolyte|electrode) reveals that only a few minutes of CELD increases the electrode activity by approximately 33 times and achieves outstanding durability with no degradation, even at 550 °C for 50 hours. Electrolyte-supported single cells are also fabricated to demonstrate the enhanced performance of the Ag electrode created *via* the ceria overcoats.

Introduction

Recently, solid oxide fuel cells (SOFCs) have been drawing much attention as a promising next-generation energy conversion device due to their high efficiency and fuel flexibility.[1,2] For sufficient oxygen-ion conductivity of the oxide electrolyte, the operating temperature of SOFCs conventionally can exceed 750 °C. However, these high operating temperatures limit the choices of materials, increase the system cost, and shorten device lifetimes.[3] Therefore, SOFCs with lower operating temperatures have been actively studied, and thin-film-based SOFCs (TF-SOFCs) which take advantage of advances in microfabrication techniques have been suggested.[4,5] Thin-film electrolytes on the scale of a few hundred nanometers allow operating temperatures as low as 450 °C and can be embedded into portable devices.[5–7]

After down-scaling the thickness of the electrolyte, the ohmic resistance can be decreased to a sufficiently low level. However, as the operating temperature is lowered, the increased cathodic polarization resistance from the sluggish oxygen reduction reaction (ORR) kinetics becomes more prominent than the ohmic resistance. Thus, the key challenge in relation to TF-SOFCs is to find a suitable material for the cathode with outstanding catalytic activity toward the ORR, electronic conductivity, and thermal/chemical stability.

While many perovskite-based oxides, such as Sr(Ti,Fe)O_3,[8–10] (La,Sr)MnO_3,[11–13] (La,Sr)(Co,Fe)O_3,[13–15] and (Ba,Sr)(Co,Fe)O_3,[16–18] have been thoroughly studied in relation to SOFC cathodes, the ORR activity is poor at lower temperatures (<450 °C) due to the high activation energy levels (1.5–2 eV) of the materials. Moreover, very high calcination temperatures are required during the manufacturing process, which can result in mechanical failures of thin-film components. On the other hand, given its superior catalytic activity at lower temperatures and high electronic conductivity, many researchers have investigated nanoporous platinum (Pt) as a TF-SOFC cathode material, but the high price and limited reserves of Pt remain as the greatest obstacles.[19]

In this regard, silver (Ag) has drawn considerable attention due to its relatively low cost, at approximately 1/50th the price of Pt (Ag: 0.58 $\$\cdot g^{-1}$, Pt: 30.1 $\$\cdot g^{-1}$),[20] as well as its excellent catalytic activity toward the ORR,[21–24] high electronic conductivity, and the process compatibility with micro-fabrication

Department of Materials Science and Engineering, Korea Advanced Institute of Science and Technology (KAIST), 291 Daehak-ro, Yuseong-gu, Daejeon 34141, Republic of Korea. E-mail: wcjung@kaist.ac.kr; Fax: +82-42-350-3310; Tel: +82-42-350-3314

† Electronic supplementary information (ESI) available. See DOI: 10.1039/d0ta02439b

‡ Current address: Department of Materials Science and Engineering, Massachusetts Institute of Technology (MIT), 77 Massachusetts Avenue, Cambridge, Massachusetts 02139, USA.

§ Current address: Korea Institute of Energy Research, Daejeon 34129, Republic of Korea.

techniques. Ag cathodes are easy to fabricate with room-temperature sputtering[25–29] or inkjet printing,[30–33] enabling the deposition of porous Ag films without a high-temperature annealing process. At the operating temperatures of SOFCs, the ORR is known to take place in the limited region near the triple-phase boundaries (TPBs) of Ag cathodes, where the Ag electrode, the electrolyte, and the oxygen gas are in contact.[27,34] Thus, it is important for fabricated nanoporous Ag electrodes to have high TPB site density levels. However, due to its low melting temperature, thermal agglomeration of Ag occurs at relatively low temperatures close to 250 °C,[35] quickly reducing the number of reaction sites and degrading the current-collecting ability, thus limiting the possible applications of Ag electrodes.

A common strategy to used extend the reaction sites and prevent thermal agglomeration is to coat the Ag thin films with thermally stable oxygen ion-conducting oxides such as yttria-stabilized zirconia (YSZ),[26,29] scandia-stabilized zirconia,[27] and samarium-doped ceria.[30–32] Several studies have shown that this can be facilitated through various coating methods, such as aerosol-assisted chemical vapor deposition (AACVD),[25] atomic layer deposition (ALD),[28,29] sputtering[26,27] or infiltration.[30,31] However, AACVD and ALD require complex systems with non-commercialized and/or precious precursors. On the other hand, high-temperature heat treatments on the order of a few hours are needed for sputtering and infiltration methods, which can cause structural failures in the thin-film components. Therefore, the development of a new approach with which the reaction sites of Ag cathodes are increased and preserved that is also simple, fast, cost-effective, and works at room temperature is crucial.

Here, we propose cathodic electrochemical deposition, referred to as CELD in this study, as a new strategy by which to add a coating of $(Pr,Ce)O_{2-\delta}$ (PCO) to Ag cathodes for stabilization. With only a simple three-electrode system, aqueous solutions and nitrate precursors, a gas-permeable and catalytically active PCO overcoat can be obtained within one minute *via* CELD.[36] The CELD process is very simple, rapid, and cost-effective compared to other well-known deposition methods.[37–40] Additionally, a subsequent annealing step to form a stable and active layer is unnecessary, making this process feasible for use with TF-SOFC fabrication processes. Similar to other doped ceria, PCO has advantages as a coating material given its favorable catalytic activity and good sintering resistance.[41–43] Its mixed conductivity in an oxidizing atmosphere extends the reaction sites to its surface, and recent studies have also implied that PCO is a promising SOFC cathode component.[36,44–46]

In the present study, we deposited PCO onto sputtered Ag thin-film electrodes *via* CELD and analyzed their microstructures and chemical compositions by means of electron microscopy, X-ray diffraction, and mass spectrometry. A remarkable improvement in the ORR activity was confirmed by electrochemical tests using both symmetric cells and single cells, demonstrating that this strategy can be used to create high-performance TF-SOFC electrodes.

Experimental

Fabrication of Ag–PCO composite films *via* CELD

Onto (100) single-crystal YSZ electrolyte substrates ($10 \times 10 \times 0.5$ mm^3, MTI Korea), 400 nm-thick nanoporous Ag electrodes were deposited by DC magnetron sputtering. The sputtering utilized a three-inch Ag target at a DC power of 100 W in an argon atmosphere while maintaining a working pressure of 60 mTorr.

Ag–PCO composite cathodes were fabricated by depositing PCO onto Ag thin film electrochemically. The CELD bath used here was based on an ethanol–water solution with a volumetric ratio of 20 : 80. Nitrate-based cation precursors, cerium(III) nitrate hexahydrate ($Ce(NO_3)_3 \cdot 6H_2O$, 99.99%, Kanto Chemical Co., Inc.) and praseodymium(III) nitrate hexahydrate ($Pr(NO_3)_3 \cdot 6H_2O$, Aldrich), were dissolved into the 60 ml bath with a total cation molar concentration of 0.05 M. The ratio of Ce to Pr was controlled when depositing the $Pr_{0.2}Ce_{0.8}O_{2-\delta}$ film. In this study, a Pr concentration of nearly 20% was chosen to maximize both the ionic and electronic conductivity levels at a pO_2 level of approximately 10^{-1} atm.[44,45] Before applying the bias, 300 sccm of oxygen gas was blown into the bath for at least 30 minutes to saturate the oxygen gas molecules in the solution. A traditional three-electrode system was employed with a standard calomel electrode (SCE, +0.24 V *vs.* standard hydrogen electrode (SHE), Koslow) for a reference electrode and a carbon rod as a counter electrode. Electrical contact with the porous Ag film was made using a tailor-made aluminum clip, which served as a working electrode. At room temperature, a bias of −0.5 V was applied between the working electrode and the reference electrode to the Ag films using a VSP-300 device (Biologic) to conduct CELD. After the electrochemical deposition process, the cell was dried, rinsed with deionized water to remove the remnants, and dried under air again before the physical and electrochemical characterizations.

Cell fabrication process

Symmetric cells (electrode|electrolyte|electrode) were fabricated to compare the ORR activities of the electrodes with respect to the CELD time. Onto both sides of (100) single-crystal YSZ substrates, Ag thin film was sputter-deposited and CELD was conducted (Fig. 1).

To examine the effect of CELD on the single-cell performance, electrolyte-supported cells with a bare Ag cathode and a CELD-treated cathode were also fabricated. Both single cells had the same electrolyte and anode for a proper comparison of the activity of the cathodes. To simplify the single-cell test, electrolyte-supported cells were utilized as the measurement platform, although the overall cathode fabrication technique proposed in this study can be applied to thin-film cells as well. To create a dense Gd-doped CeO_2 (GDC) electrolyte pellet, GDC nano-powder (GDC10, fuelcellmaterials) was uniaxially pressed at 5 MPa with a 13×13 mm^2 square die mold and sintered at 1450 °C for ten hours. By controlling the mass of the powder, the thickness of the GDC pellet was set to approximately 350 μm. Then, in order to minimize the effect of anode polarisation on the

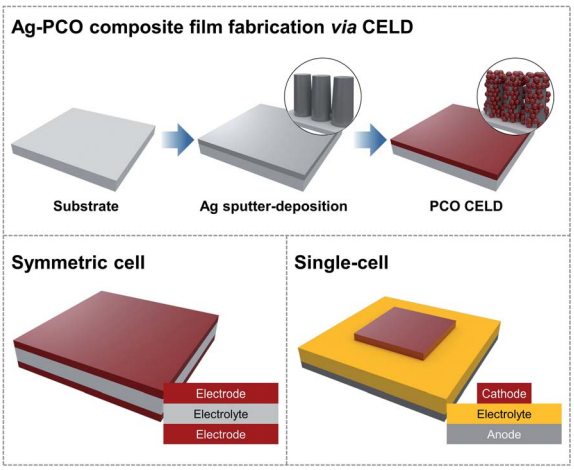

Fig. 1 Schematic procedure used to deposit PCO onto sputter-deposited Ag thin film *via* CELD. The structures of the fabricated cells are shown below.

overall cell performance, nanoporous Pt films were also deposited by DC magnetron sputtering. The thickness of the nanoporous Pt anode was set to approximately 200 nm following a previous study reporting that a Pt anode created under this fabrication condition has superior activity (~0.1 Ω cm² at 450 °C).[27]

Physical/chemical characterizations

The structures of the electrodes were investigated by scanning electron microscopy (SEM, Hitachi S-4800). Because some of the sample surfaces were insulating, carbon tape and osmium coatings were put onto the surfaces to avoid electron charging effects. Both top-view and cross-section images were obtained. In general, an electron acceleration voltage of 7–10 kV was used to obtain images at high resolutions. The working distance was set to approximately 5 mm.

To investigate the interfaces between the Ag and the oxides, transmission electron microscopy (TEM, 300kV-Tecnai G2 F30 S-Twin) was used. Onto a clean surface of a fabricated GDC pellet, 400 nm-thick nanoporous Ag film was sputter-deposited, followed by 60 seconds of PCO CELD. The sample was prepared using a focused ion beam (FIB) for a TEM analysis. To obtain high-resolution cross-sectional TEM images, an acceleration voltage of 300 kV was used. The elemental composition of the sample was also characterized in line-scanning mode with an energy-dispersive X-ray spectroscope (EDX).

A thin-film X-ray diffraction (XRD, Rigaku Ultima IV) analysis was conducted to confirm that the CELD process results in the deposition of PCO without significant second phases. To analyze the diffraction patterns of PCO, the samples were prepared on single-crystal Si ($10 \times 10 \times 0.5$ mm^2, Siltron). A Cu-Kα X-ray ($\lambda = 0.15418$ nm) source was radiated at 40 kV and 40 mA. The theta-two theta mode was used for two theta = 20–60° with a scan rate of $2^\circ \cdot \mathrm{min}^{-1}$ and a step size of 0.01°.

Inductively coupled plasma mass spectrometry (ICP-MS, Agilent ICP-MS 7700S) was utilized to measure the composition of the deposited PCO film. CELD was held at −0.5 V for 10 minutes and the Ag–PCO composite film was delaminated from the Si substrate for the analysis. Microwave digestion in 30 ml of 70% nitric acid and 70 ml of 35% hydrochloric acid at 200 °C for three minutes preceded this process. The concentrations of Pr and Ce were measured at the ppm level.

Electrochemical characterizations

Symmetric cells were placed in alumina tubes and electrical contact was made using clip-type Pt wires. While maintaining $pO_2 = 0.21$ atm, AC impedance spectroscopy (ACIS) with 20 mV perturbation was conducted at 450–350 °C using a VSP-300 device. From the spectra, the electrode activities were extracted at each temperature.

For the single-cell tests, the fabricated cells were placed onto a custom-made single-cell measurement system. A Pt mesh was placed onto each electrode for current collection. An alumina-based ceramic sealant (Ceramabond 503, Aremco) was deposited along the circumference of the cell for sealing, after which 50 sccm of synthetic air with an N_2-to-O_2 ratio of 79 : 21 was fed into the cathode side and 50 sccm of wet hydrogen with 3 vol% water vapor was fed into the anode side. The entire station in the quartz tube was placed into a vertical tube furnace to adjust the operating temperature of the cell. Drying and curing of the sealant were performed by holding the temperature at 93 °C for two hours and then at 260 °C for two hours. The ramping rate was always held to less than 4 °C min^{-1} to prevent any mechanical fracture of the cell. Current density–voltage–power density (*I–V–P*) curves were obtained by a potentiostat with a 20 mV s^{-1} scanning rate, and the peak power densities of the cells were compared.

Results & discussions

Microstructure and composition of Ag–PCO composite films

The sputter-deposited nanoporous Ag films with and without the CELD-overcoat on a Si wafer were observed by SEM (Fig. 2). The Ag film has a columnar structure with nanoscale pores. The columns are interconnected with very high TPB densities. The thickness of each film is approximately 400 nm. After PCO was electrochemically deposited onto the Ag film and dried, the PCO film covered the Ag columns with a flake-like appearance. No significant delamination or collapse of the structure due to the

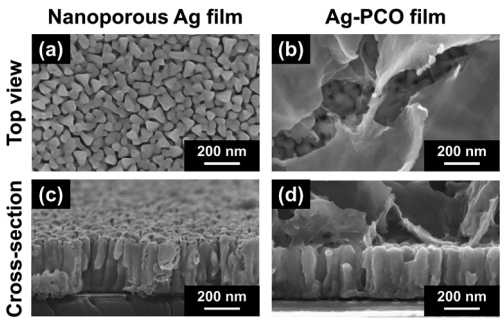

Fig. 2 The (a and b) top-view and (c and d) cross-section SEM images of the sputter-deposited (a and c) nanoporous Ag film and (b and d) CELD-treated Ag–PCO film samples.

CELD process arose. In the top-view image of the Ag–PCO film, micrometer-scale cracks were observed; such cracks are known to form during the drying step due to the volumetric difference of $(Pr,Ce)(OH)_3$ and PCO.

Because SEM presents limitations when studying the detailed morphology of Ag–PCO films, a TEM analysis was also undertaken to observe the interfaces (Fig. 3). The Ag columns were shown to be uniformly covered with the PCO coating. Supported by interplanar distance measurements of the Ag (200) and PCO (100) planes (0.203 and 0.313 nm, respectively), the PCO coating was confirmed to have penetrated into the pores of the Ag columns. The EDX line scan profile is in good agreement with the image shown in Fig. 3(c). The nonzero Ce signal intensity in the Ag column region (200–450 nm) implies that the PCO coating is present inside the pores of the Ag film. This penetrated PCO layer is expected physically to prevent the agglomeration of the Ag film and to provide conduction pathways for oxygen ions.

XRD patterns of the Ag and Ag–PCO films are shown in Fig. 4. The bare Ag sample shows a significant (111) peak at 38.08° with a slightly smaller (200) peak at 44.36°, which are the featured peaks of Ag. The very small peaks near 34° and 37° originate from the Ag_2O and AgO phases which formed due to the slight oxidation of the Ag surface. No noticeable change in the diffraction pattern was observed just after the CELD process, meaning that the as-deposited film is amorphous. However, after the ten-hour heat treatment at 450 °C, a strong PCO (200) peak and a weak PCO (111) peak were observed. These diffraction angles are well-matched with previously reported data.[47]

The chemical composition as measured by ICP-MS in Table 1 shows that the composition of Pr in the film was close to 20.1%. As expected given that $Pr(OH)_3$ is less soluble than $Ce(OH)_3$, the content of Pr was higher in the CELD film than in the CELD bath. The resulting content of 20% is an ideal doping concentration of Pr to maximize the conductivity of PCO.[45]

Electrochemical activity of Ag–PCO composite films

During the CELD processes lasting 30, 45, and 60 seconds, the electrical current continues to flow in the three-electrode system, resulting in corresponding electrical charges of 37, 51, and 62 mC cm^{-2}. Accordingly, we refer to these Ag–PCO films as Ag–PCO37, Ag–PCO51, and Ag–PCO62, respectively.

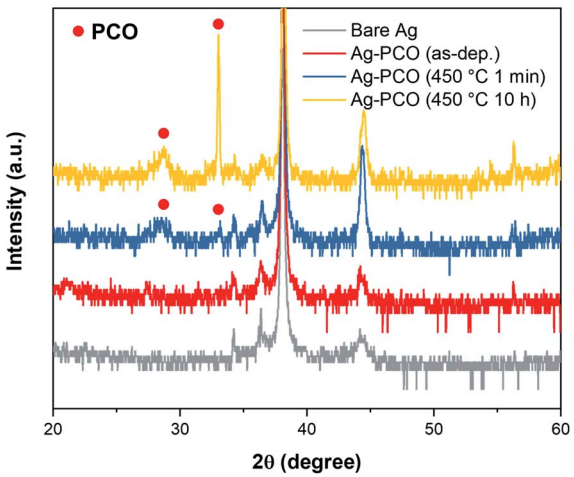

Fig. 4 XRD patterns of bare Ag and Ag–PCO films on a (100) single-crystal Si substrate before and after 450 °C annealing for one minute and ten hours.

Fig. 5(a) depicts the impedance spectra of the symmetric cells measured at 450 °C while holding the oxygen partial pressure (pO_2) at 0.21 atm. The typical impedance spectra of symmetrical cells are composed of two semicircles. The high-frequency arc is mainly attributed to the ohmic resistance from the electrolyte. To simplify the comparison of the electrode activity, only the low-frequency semicircles were placed on the origin of the graph. The diameter of the semicircle represents the polarization resistance of the electrodes. Thus, it was found that the electrode resistance value decreased in the order of bare Ag > Ag–PCO62 > Ag–PCO37 > Ag–PCO51. Noting that the frequency at the apex of the semicircle is the reciprocal of the resistance multiplied by the double-layer capacitance, the Ag–PCO composite electrodes had much lower frequencies, meaning that the PCO coatings increased the double-layer capacitance to a considerable degree. This increased double-layer capacitance is attributed to the increased charge separation at the interfacial active sites. This result is in good agreement with the hypothesis that electrochemically deposited PCO coatings with microscale cracks extend the reaction sites from Ag|electrolyte|air to Ag|PCO|air.

From the impedance spectra obtained at 450–350 °C while maintaining $pO_2 = 0.21$ atm, the electrode activity, which is the

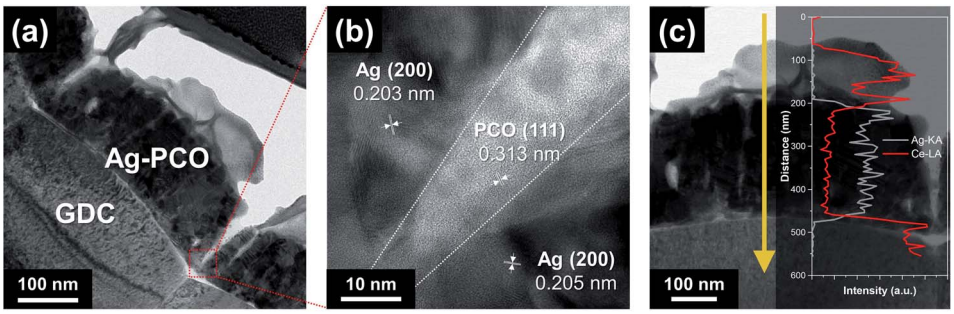

Fig. 3 Cross-section TEM images of (a) PCO-coated Ag film deposited at −0.5 V *vs.* SCE for 60 seconds, (b) the atomic-scale feature of the PCO|Ag and PCO|GDC interfaces. (c) The EDX line scan profile following the red arrow is shown.

Table 1 ICP-MS compositional analysis of the PCO solution and film

	Pr concentration (%)
CELD bath	15.0
CELD film	20.1 ± 0.1

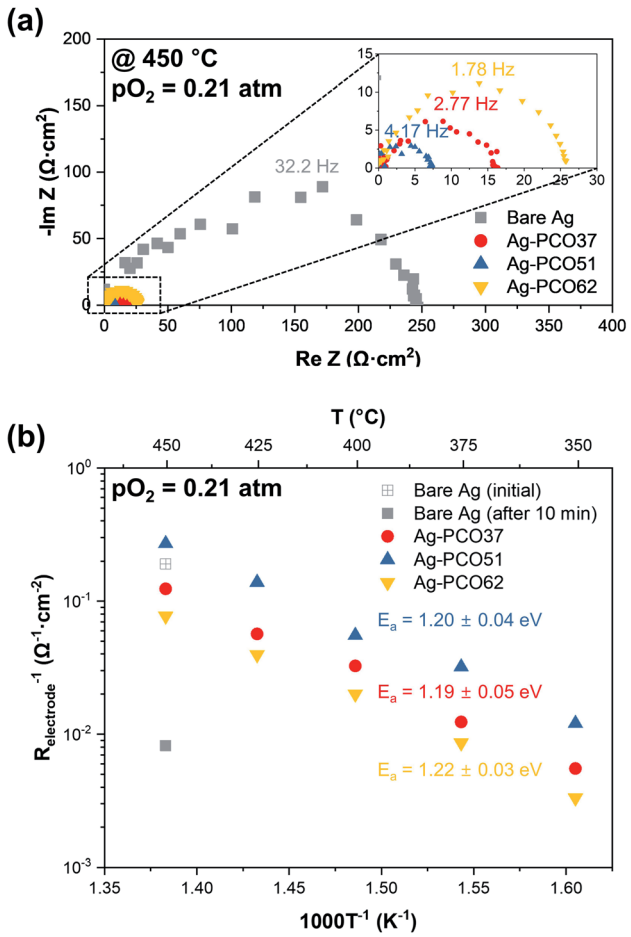

Fig. 5 (a) The AC impedance spectra of the symmetric cells (bare Ag, Ag–PCO37, Ag–PCO51, Ag–PCO62) obtained at 450 °C while maintaining the oxygen partial pressure at 0.21 atm (the offset resistance is omitted to simplify the comparison). (b) The electrode activities obtained at 450–350 °C, while the bare Ag cell was only analyzed at 450 °C due to rapid degradation.

reciprocal of the polarisation resistance normalized by the nominal electrode area, was determined, as depicted in Fig. 5(b). The degradation rate of the bare Ag cell was rapid such that only the electrode activity at 450 °C after ten minutes of stabilization could be plotted. After ten minutes, the bare Ag electrode activity was stabilized, and the value was approximately $8.23 \times 10^{-3}\ \Omega^{-1}\ cm^{-2}$ at 450 °C with $pO_2 = 0.21$ atm. On the other hand, the Ag–PCO51 electrode, which was CELD-treated only for 45 seconds, showed activity of $2.70 \times 10^{-1}\ \Omega^{-1}\ cm^{-2}$, 33 times higher. The Ag–PCO37 and Ag–PCO62 samples also showed sizable activity improvements compared to the bare Ag electrode, but the optimal condition was 51 mC cm^{-2}. This likely occurred because as more PCO was coated, the reaction site gradually increases and the sites then began to be passivated by the excess coating. A similar result was reported for CELD-treated Pt/Sm-doped CeO_2 composite electrodes.[37] Indeed, the activation energy of each electrode showed the same value of 1.20 eV within an acceptable margin of error, further supporting that the change in the electrode activity with the PCO coating time is simply due to the change in the number of active sites (Fig. 5(b)).[33]

Next, we analyzed the evolution of the electrode activation over time to confirm the durability of the bare Ag and Ag–PCO51 samples (Fig. 6). As mentioned earlier, the bare Ag cell degraded rapidly, most likely due to severe thermal agglomeration such that the activity decreased by more than 20 times in approximately ten minutes. Moreover, the ohmic resistance, which is the sum of electrolyte ohmic resistance and the in-plane resistance of the Ag thin film, also increased rapidly. This occurred because the Ag thin films were disconnected and formed isolated islands on the YSZ substrate. This is known to be a 'fatal issue', after which Ag thin films cannot be used as TF-SOFC electrodes.[35] In contrast, the ohmic resistance of the Ag–PCO51 cell showed no degradation for 50 hours, even at 550 °C. Furthermore, the electrode activity actually slightly increased under the same condition. According to the literature, an electrochemically deposited doped-ceria coating is known to form

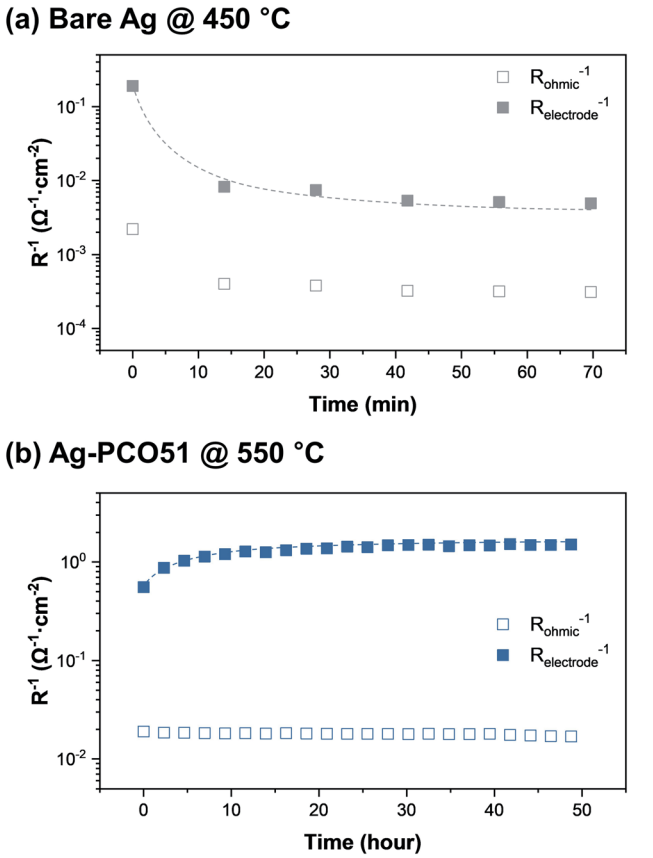

Fig. 6 Long-term stability test results by comparing the change in the electrode activity of (a) bare Ag cell at 450 °C and (b) Ag–PCO51 cell at 550 °C.

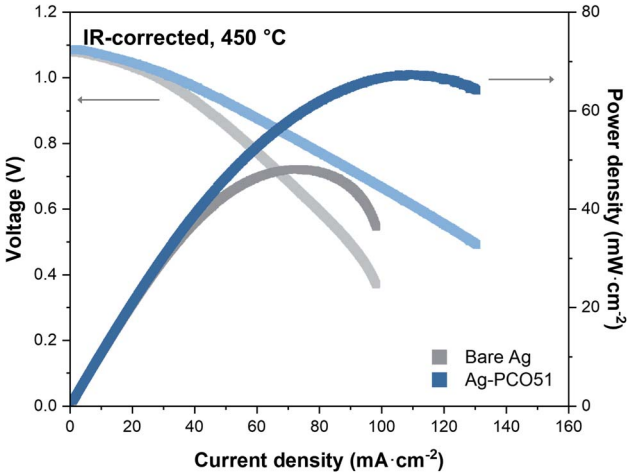

Fig. 7 *IR*-corrected *I–V–P* curves of single-cells with bare Ag and Ag–PCO51 cathodes measured at 450 °C.

microscale cracks continuously at an elevated temperature, and such cracks may have increased the density of the reaction sites.[36,37] It should be noted that, to the best of our knowledge, this study is the very first report on the stable operation of Ag thin-film cathodes at temperatures as high as 550 °C.

Finally, to demonstrate the effect of CELD to the performance enhancement of SOFCs, single cells with the bare Ag and Ag–PCO51 cathodes were compared. The single cells were electrolyte-supported, and the high ohmic resistances caused by the thick electrolyte (nearly occupying 80% of the total resistance) made it difficult to compare the effects of the electrode improvement. Therefore, the *I–V–P* curves shown in Fig. 7 were *IR*-corrected, *i.e.*, plotted without the ohmic contribution to the voltage loss. The open-circuit voltages of the bare Ag and Ag–PCO51 single cells were 1.076 and 1.080 V, respectively, within the acceptable range of the margin of error. Noting that there is no significant concentration polarisation on the Ag–PCO51 single cell, the PCO coating *via* CELD is sufficiently gas-permeable due cracking which arose during the drying and annealing steps. The ohmic-resistance-free peak power density of the Ag–PCO single cell was approximately 67.4 mW cm^{-2}, which is nearly 40% higher than that of the bare Ag single cell (48.2 mW cm^{-2}). This improvement is quite remarkable considering that CELD is a room-temperature, non-vacuum, and time-efficient (*i.e.*, one minute) process.

Conclusion

In this work, we analysed and evaluated Ag cathodes coated with PCO for application to TF-SOFCs. The PCO overcoating was deposited onto a porous Ag film by CELD, which is a fast, simple, cost-effective, room-temperature deposition technique. Structural and compositional studies were undertaken by SEM, TEM, ICP-MS, and XRD. The ORR activities of the electrodes were compared with symmetric cell tests, followed by single-cell tests to demonstrate that CELD can effectively enhance the performance and stability of TF-SOFC cathodes. Impedance spectroscopy results showed that the Ag–PCO cathodes outperformed bare Ag cathodes. Only 45 seconds of the CELD process resulted in 33-fold improved electrode activity. This reduction of the cathodic polarisation resistance led to an increase in the *IR*-corrected peak power density of a single cell from 48.2 to 67.4 mW cm^{-2} at 450 °C. Long-term measurements confirmed that CELD ensures superior thermal stability of Ag cathodes, allowing them to withstand use without any degradation, even at 550 °C for 50 hours. In sum, the CELD method as described here is suggested as a possible solution to achieve both high performance and long-term stability of TF-SOFC cathodes.

Conflicts of interest

There are no conflicts to declare.

Acknowledgements

This work was financially supported by the Korea Institute of Energy Technology Evaluation and Planning (KETEP) and the Ministry of Trade, Industry and Energy (MOTIE) of the Republic of Korea (No. 20173020032120 and No. 20163030031850). We also thank Prof. Jung-Sik Kim of Loughborough University for the review of our work.

References

1 Z. Shao and S. M. Halle, *Nature*, 2004, **431**, 170–173.
2 Y. Choi, S. K. Cha, H. Ha, S. Lee, H. K. Seo, J. Y. Lee, H. Y. Kim, S. O. Kim and W. Jung, *Nat. Nanotechnol.*, 2019, **14**, 245–251.
3 E. D. Wachsman and K. T. Lee, *Science*, 2011, **334**, 935–939.
4 J. An, J. H. Shim, Y.-B. Kim, J. S. Park, W. Lee, T. M. Gür and F. B. Prinz, *MRS Bull.*, 2014, **39**, 798–804.
5 H. L. Tuller, S. J. Litzelman and W. Jung, *Phys. Chem. Chem. Phys.*, 2009, **11**, 3010.
6 I. Chang, J. Bae, J. Park, S. Lee, M. Ban, T. Park, Y. H. Lee, H. H. Song, Y. B. Kim and S. W. Cha, *Energy*, 2016, **104**, 107–113.
7 D. Beckel, A. Bieberle-Hütter, A. Harvey, A. Infortuna, U. P. Muecke, M. Prestat, J. L. M. Rupp and L. J. Gauckler, *J. Power Sources*, 2007, **173**, 325–345.
8 W. Jung and H. L. Tuller, *Adv. Energy Mater.*, 2011, **1**, 1184–1191.
9 B. Koo, K. Kim, J. K. Kim, H. Kwon, J. W. Han and W. Jung, *Joule*, 2018, **2**, 1476–1499.
10 B. Koo, H. Kwon, Y. Kim, H. G. Seo, J. W. Han and W. Jung, *Energy Environ. Sci.*, 2018, **11**, 71–77.
11 W. Wang and S. P. Jiang, *Solid State Ionics*, 2006, **177**, 1361–1369.
12 S. P. Jiang, *J. Mater. Sci.*, 2008, **43**, 6799–6833.
13 F. S. Baumann, J. Fleig, M. Konuma, U. Starke, H.-U. Habermeier and J. Maier, *J. Electrochem. Soc.*, 2005, **152**, A2074.
14 A. Mai, V. A. C. Haanappel, S. Uhlenbruck, F. Tietz and D. Stöver, *Solid State Ionics*, 2005, **176**, 1341–1350.

15 A. Esquirol, N. P. Brandon, J. A. Kilner and M. Mogensen, *J. Electrochem. Soc.*, 2004, **151**, 1847–1855.
16 Y. Lin, R. Ran, Y. Zheng, Z. Shao, W. Jin, N. Xu and J. Ahn, *J. Power Sources*, 2008, **180**, 15–22.
17 W. Zhou, R. Ran and Z. Shao, *J. Power Sources*, 2009, **192**, 231–246.
18 H. Zhao, W. Shen, Z. Zhu, X. Li and Z. Wang, *J. Power Sources*, 2008, **182**, 503–509.
19 W. Jung, J. J. Kim and H. L. Tuller, *J. Power Sources*, 2015, **275**, 860–865.
20 *Precious and Industrial Metals – Bloomberg*, accessed, 26 February 2020, https://www.bloomberg.com/markets/commodities/futures/metals.
21 C.-C. Yu, J. Dae Baek and P.-C. Su, in *2016 IEEE 29th International Conference on Micro Electro Mechanical Systems (MEMS)*, IEEE, 2016, vol. 2016-Febru, pp. 1260–1263.
22 J. K. Nørskov, J. Rossmeisl, A. Logadottir, L. Lindqvist, J. R. Kitchin, T. Bligaard and H. Jónsson, *J. Phys. Chem. B*, 2004, **108**, 17886–17892.
23 J. H. Shim, Y. B. Kim, J. S. Park, J. An, T. M. Gür and F. B. Prinz, *J. Electrochem. Soc.*, 2012, **159**, B541.
24 D. E. Vladikova, Z. B. Stoynov, A. Barbucci, M. Viviani, P. Carpanese, J. A. Kilner, S. J. Skinner and R. Rudkin, *Electrochim. Acta*, 2008, **53**, 7491–7499.
25 H. R. Choi, K. C. Neoh, H. J. Choi, G. D. Han, D. Y. Jang, D. Kim and J. H. Shim, *J. Power Sources*, 2018, **402**, 246–251.
26 D. H. Kim, K. Bae, H. J. Choi and J. H. Shim, *J. Alloys Compd.*, 2018, **769**, 545–551.
27 H. J. Choi, M. Kim, K. C. Neoh, D. Y. Jang, H. J. Kim, J. M. Shin, G.-T. Kim and J. H. Shim, *Adv. Energy Mater.*, 2017, **7**, 1601956.
28 K. C. Neoh, G. D. Han, M. Kim, J. W. Kim, H. J. Choi, S. W. Park and J. H. Shim, *Nanotechnology*, 2016, **27**, 185403.
29 Y. K. Li, H. J. Choi, H. K. Kim, N. K. Chean, M. Kim, J. Koo, H. J. Jeong, D. Y. Jang and J. H. Shim, *J. Power Sources*, 2015, **295**, 175–181.
30 T.-H. Lee, L. Fan, C.-C. Yu, F. E. Wiria and P.-C. Su, *J. Mater. Chem. A*, 2018, **6**, 7357–7363.
31 T.-H. Lee, J. Baek, L. Fan, F. Wiria, P.-C. Su and S. Lee, *Energies*, 2018, **11**, 2181.
32 T.-H. Lee, K.-Y. Liu, F. E. Wiria and P.-C. Su, in *2017 IEEE/SICE International Symposium on System Integration (SII)*, IEEE, 2017, vol. 2018-Janua, pp. 83–88.
33 C. C. Yu, J. D. Baek, C. H. Su, L. Fan, J. Wei, Y. C. Liao and P. C. Su, *ACS Appl. Mater. Interfaces*, 2016, **8**, 10343–10349.
34 J. H. Wang, M. L. Liu and M. C. Lin, *Solid State Ionics*, 2006, **177**, 939–947.
35 N. J. Simrick, J. A. Kilner and A. Atkinson, *Thin Solid Films*, 2012, **520**, 2855–2867.
36 H. G. Seo, Y. Choi and W. Jung, *Adv. Energy Mater.*, 2018, **8**, 1703647.
37 H. G. Seo, Y. Choi, B. Koo, A. Jang and W. Jung, *J. Mater. Chem. A*, 2016, **4**, 9394–9402.
38 Y. Choi, E. C. Brown, S. M. Haile and W. Jung, *Nano Energy*, 2016, **23**, 161–171.
39 Y. Choi, J. Kim, H. G. Seo, H. L. Tuller and W. Jung, *Electrochim. Acta*, 2019, **316**, 273–282.
40 B.-K. Park, H. G. Seo, W. Jung and J.-W. Lee, *Ceram. Int.*, 2018, **44**, 18727–18735.
41 T.-S. Oh, Y. S. Tokpanov, Y. Hao, W. Jung and S. M. Haile, *J. Appl. Phys.*, 2012, **112**, 103535.
42 S. Lee, J. Seo and W. Jung, *Nanoscale*, 2016, **8**, 10219–10228.
43 S. Kim, S. Lee and W. Jung, *ChemCatChem*, 2019, 201900934.
44 S. R. Bishop, T. S. Stefanik and H. L. Tuller, *Phys. Chem. Chem. Phys.*, 2011, **13**, 10165–10173.
45 S. R. Bishop, T. S. Stefanik and H. L. Tuller, *J. Mater. Res.*, 2012, **27**, 2009–2016.
46 H. L. Tuller, S. R. Bishop, D. Chen, Y. Kuru, J. J. Kim and T. S. Stefanik, *Solid State Ionics*, 2012, **225**, 194–197.
47 Y. Wang, T. Mori, J.-G. Li and T. Ikegami, *J. Am. Ceram. Soc.*, 2004, **85**, 3105–3107.